PAPER

Check for updates

Synthesis of Cu/Mn/Ce polymetallic oxide catalysts and catalytic ozone treatment of wastewater

Jinlong Zhong, [*abcd] Xue feng Mao,[abcd] Guanyu Wang,[bcd] Heng Li,[bcd] Junfang Li,[bcd] Sijian Qu[abcd] and Jianwei Zhao[e]

Non-homogeneous ozone-catalyzed oxidation technology is one of the effective ways of treating wastewater, the core of which lies in the development of efficient ozone oxidation catalysts. This work proposes the design and synthesis of an efficient Cu/Mn/Ce multi-metal composite oxide catalyst by metal salt precursor mixing-direct granulation. The effect of metal doping on the catalyst properties was compared using Density function theory (DFT) calculations, and the Cu/Mn/Ce co-doping showed significant charge accumulation effect with a low ozonolysis energy barrier, which is more favorable for the generation of reactive oxygen species. The successful loading of the main active metal components, such as Mn, Cu, and Ce, was clarified by systematic characterization by X-ray diffraction (XRD), X-ray photoelectron spectroscopy (XPS), scanning electron microscopy (SEM), energy dispersive spectroscopy (EDS) and Brunauer–Emmett–Teller's test (BET), and the chemical oxygen demand (COD) removal could reach more than 60% for the simulated wastewater. The electron paramagnetic resonance (EPR) characterization clarified that the degradation of organic pollutants was mainly dominated by the combination of single-linear oxygen and superoxide radicals in the catalytic process, and the possible catalytic oxidation mechanism was proposed. This work advances the development of non-homogeneous ozone oxidation technology.

1. Introduction

Wastewater treatment is conducive to alleviate the problem of water scarcity, how to efficiently treat wastewater has attracted the attention of the majority of researchers.[1,2] At present, adsorption technology, photocatalysis and microwave catalysis technology, biochemical methods, and advanced oxidation methods are widely used in the field of wastewater treatment,[3–7] and have achieved good results. Among them, the advanced oxidation method mainly uses H_2O_2, O_3, *etc.* as oxidizing agents, and generates strong oxidizing active radicals through the action of catalysts, so as to realize the efficient degradation of organic pollutants. This technology has the advantages of strong oxidizability, small footprint, and easy operation, which has caused extensive research.[8,9]

Non-homogeneous ozone catalytic oxidation technology is one of the advanced oxidation methods, in which ozone is decomposed into strong oxidizing radicals such as hydroxyl radicals and superoxide radicals through the design and synthesis of catalysts to achieve the degradation of pollutants based on the direct oxidation of ozone and indirect oxidation of radicals.[10–12] Therefore, the core of this process lies in the design and synthesis of efficient non-homogeneous ozone oxidation catalysts.[13–16] Existing studies have mainly focused on the preparation of metal oxide catalysts, carbon-based non-metal oxide catalysts, metal–organic framework (MOF) and other catalysts, and the types and contents of metal active centers and non-metal active centers were adjusted to improve the performance of the catalysts by improving the catalyst preparation process. Currently, metal oxide catalysts are one of the most widely studied catalysts for ozone oxidation due to their good ozone catalytic performance and low cost.[17–20]

Metal oxidation catalysts are usually monometallic oxides or their loaded catalysts, which can provide electrons for ozone decomposition conversion through valence cycling of the metal centers, but the monometallic active components are easy to be leached out and lost due to the collision of catalyst particles and other factors during ozone-catalyzed oxidation, resulting in a decrease in the effect of the catalyst.[21] Therefore, researchers have proposed doping and other modifications to improve the catalyst performance by introducing different active metal components while inhibiting the loss of active components, which has achieved better results. It is worth noting that the current doping through the conventional experimental comparison, the workload is large, and the mechanism of doping modification and

a China Coal Research Institute, Beijing 100013, China. E-mail: 61865298@qq.com; Tel: +86-10-84262941

b China Coal Research Institute Corporation Ltd., Beijing 100013, China

c National Energy Technology & Equipment Laboratory of Coal Utilization and Emission Control, Beijing 100013, China

d Beijing Key Laboratory of Coal Based Carbon Materials, Beijing 100013, China

e Shenzhen HUASUAN Technology Co., Ltd, Beijing 100013, China

the catalyst properties caused by the catalyst has not been studied in depth, there is an urgent need to further through the combination of computational and experimental means to screen the dopant metal and reveal its mechanism of action.[22,23]

In this work, a design and preparation study of a multimetallic oxide catalyst by DFT calculations combined with experiments is proposed. Based on the results of DFT calculations, an efficient Cu/Mn/Ce multimetallic ozone oxidation catalyst was designed and synthesized by metal salt precursor mixing-direct granulation. The conformational relationship of the catalyst was revealed by XRD, BET and other systematic characterizations. Finally, the EPR characterization clarified that the degradation of organic pollutants in the catalytic process was mainly dominated by single-linear oxygen and superoxide radicals, and proposed the possible catalytic oxidation mechanism, which provided a reference for the synthesis of new efficient ozone oxidation catalysts.

2. Methods

2.1 Reagents

Manganese nitrate, copper nitrate, cerium nitrate, and Al_2O_3 powder were purchased from Shanghai McLean Co. Phenol (99%), pyridine (99%), quinoline (99%) and nitrobenzene (99%) were purchased from Shanghai Aladdin Co. The drugs used were used directly without further purification, and ultrapure water (18.2 Ω) was used as solvent for solution configuration.

2.2 Catalyst preparation

Weigh a certain mass of manganese nitrate, copper nitrate, cerium nitrate, added to ultrapure water, fully stirred for 1 h and then added Al_2O_3 powder, fully mechanically stirred for 6 h and then put into the granulator for catalyst molding preparation (control particle size of 3–5 mm), the precursor of the catalyst samples obtained was dried in an 80 °C oven for 12 h and then put into a muffle furnace for 4 h calcined in an air atmosphere of 500 °C, and finally Cu/Mn/Ce multi-metal composite oxide catalyst was obtained.

2.3 Batch experiment

The steps of catalytic oxidation experiment are as follows: take 1 L of simulated wastewater (phenol (50 mg L^{-1}), pyridine (10 mg L^{-1}), quinoline (10 mg L^{-1}), nitrobenzene (10 mg L^{-1}) are the main pollutants, the initial COD concentration is about 250 mg L^{-1}), add a certain amount of catalyst, the reaction device is a glass column (inner diameter of 4 cm, height of 1.5 m), and the wastewater is circulated by a peristaltic pump in order to be mixed uniformly. Control ozone generator outlet O_3 gas flow rate of 0.2–0.4 L min^{-1}, O_3 gas concentration (20–80) mg L^{-1}, every period of time to take samples to analyze the COD concentration changes.

2.4 Characterization method

The XRD test was carried out using an X-ray diffractometer (Bruker D8 advance), the target material was copper target, the scanning range was 10–80°, and the scanning speed was 5° min^{-1}. The specific surface area of the catalyst was determined using a specific surface area and porosity analyzer (ASAP2460) from Micromeritics, U.S.A. X-ray photoelectron spectrometer (Thermo Scientific Escalab 250Xi) was used for the test, in which the vacuum degree of the analyzing chamber was 5×10^{-9} mBar, the excitation source was Alka rays ($hv = 1486.6$ eV), the working voltage was 12 kV, the filament current was 6
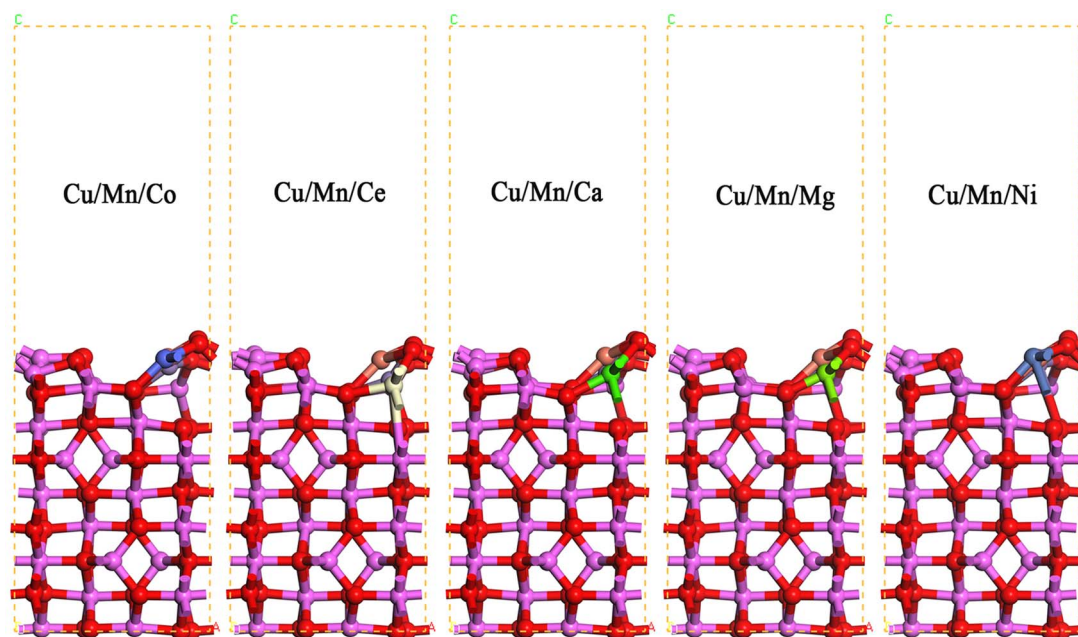

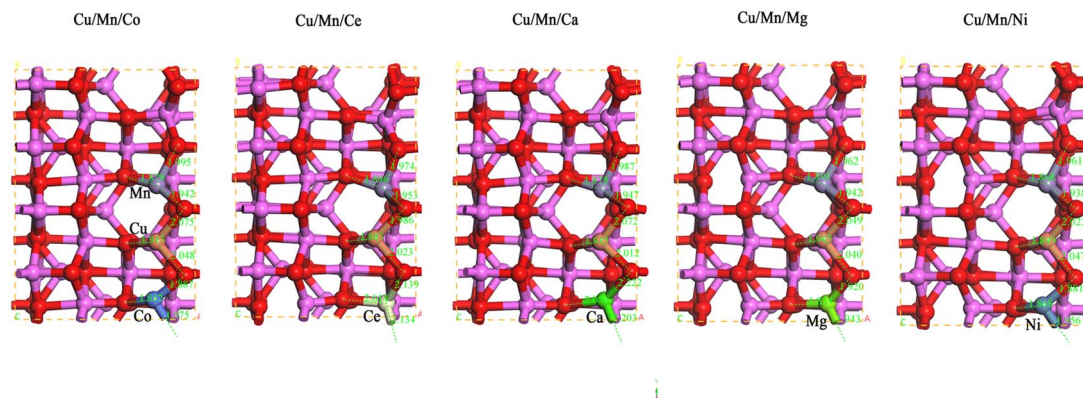Fig. 1 Surface model of γ-Al_2O_3 modified by Cu/Mn/Co, Cu/Mn/Ce, Cu/Mn/Ca, Cu/Mn/Mg and Cu/Mn/Ni doping.

Fig. 2 Schematic diagram of bond length of γ-Al₂O₃ surface model modified by Cu/Mn/Co, Cu/Mn/Ce, Cu/Mn/Ca, Cu/Mn/Mg and Cu/Mn/Ni doping.

mA, and the C 1s = 284.80 eV binding energy was used as the energy standard. Charge correction was performed.

2.5 Calculation method

All calculations were simulated using the CASTEP software package in Materials Studio. Based on the generalized gradient approximation (GGA) plane wave pseudopotential method under DFT, the Perdew–Burke–Ernzerhof (PBE) density functional description[24] is chosen and the ultrasoft pseudopotentials (USP) is used to describe the Kohn–Sham (K–S) plane wave pseudopotentials. USP are used to solve the Kohn–Sham (K–S) equations and energy functionals in a self-consistent (SCF) manner. The plane-wave truncation energy is set to 380 eV, the convergence accuracy of the self-concordant field is 2.0×10^{-5} eV atm^{-1}, the internal stress is not greater than 0.1 GPa, and the *k*-points in the Brillouin zone are taken as $3 \times 2 \times 2$.

3. Results and discussion

3.1 Catalyst design

In the cell of Cu/Mn bimetallic dopant-modified γ-Al₂O₃(020), the other surface Al atoms adjacent to Cu were replaced by Co, Ce, Ca, Mg, and Ni atoms, respectively, to construct five different tri-metallic dopant-modified γ-Al₂O₃ surface models,

and to optimize the structure, and the optimized obtained models are shown in Fig. 1. As can be seen in Fig. 2, after Cu/Mn/Co doping modified γ-Al₂O₃, the bond lengths of Cu and adjacent O atoms are 1.913 Å, 2.075 Å, 2.048 Å, the bond lengths of Mn and adjacent O atoms are 1.879 Å, 1.995 Å, 1.942 Å, the bond lengths of Co and adjacent O atoms are 1.852 Å, 1.887 Å, 1.975 Å; the bond lengths of Cu/Mn and adjacent O atoms are 1.852 Å, 1.887 Å, 1.975 Å; and the bond lengths of Cu/Mn and
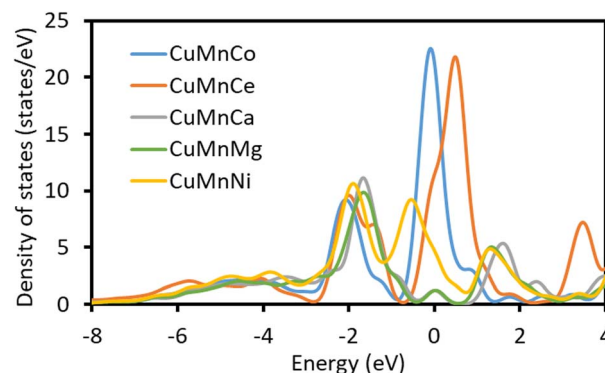

Fig. 4 DOS of γ-Al₂O₃ modified by Cu/Mn/Co, Cu/Mn/Ce, Cu/Mn/Ca, Cu/Mn/Mg and Cu/Mn/Ni doping.
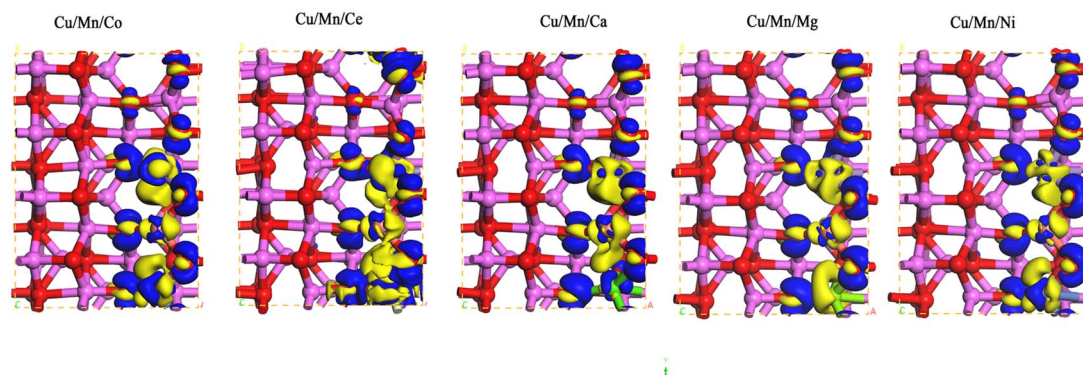

Fig. 3 Charge density difference of γ-Al₂O₃ surface model modified by Cu/Mn/Co, Cu/Mn/Ce, Cu/Mn/Ca, Cu/Mn/Mg and Cu/Mn/Ni doping.
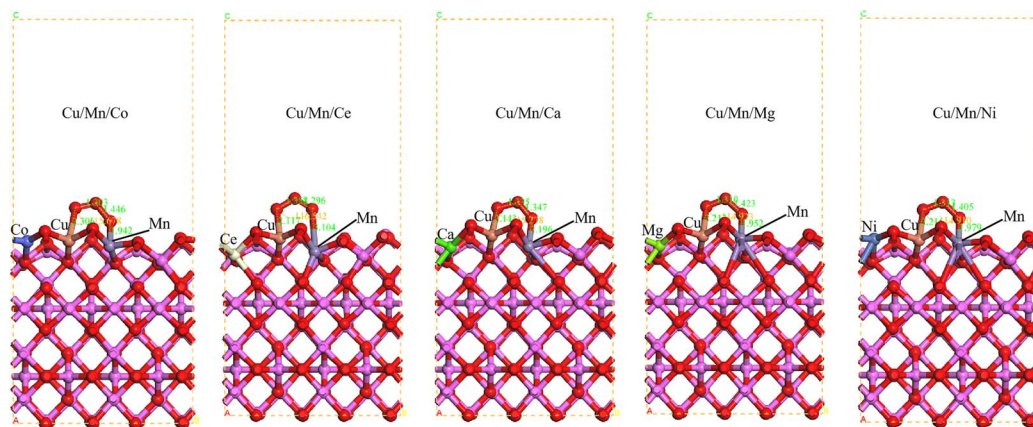
Fig. 5 O_3 adsorption configurations of γ-Al$_2$O$_3$ surface modified by Cu/Mn/Co, Cu/Mn/Ce, Cu/Mn/Ca, Cu/Mn/Mg and Cu/Mn/Ni doping.

adjacent O atoms are 1.852 Å, 1.887 Å, 1.975 Å; Cu/Mn/Ce doped modified γ-Al$_2$O$_3$, the bond lengths of Cu and neighboring O atoms are 1.883 Å, 1.986 Å, 2.023 Å, the bond lengths of Mn and neighboring O atoms are 1.886 Å, 1.974 Å, 1.953 Å, the bond lengths of Ce and neighboring O atoms are 2.014 Å, 2.139 Å, 2.134 Å, and Cu/Mn/Ca doped modified γ-Al$_2$O$_3$ is 1.995 Å, 1.942 Å, and Co and neighboring O atoms are 1.852 Å, 1.887 Å, 1.975 Å, respectively. Mg doping modified γ-Al$_2$O$_3$, the bond lengths of Cu and neighboring O atoms are 1.905 Å, 2.049 Å, 2.040 Å, the bond lengths of Mn and neighboring O atoms are 1.891 Å, 1.962 Å, 1.942 Å, and the bond lengths of Mg and neighboring O atoms are 1.854 Å, 1.920 Å, 1.943 Å; Cu/Mn/Ni doping modified γ-Al$_2$O$_3$, the bond lengths of Ca and neighboring O atoms are 2.056 Å, 2.222 Å, 2.203 Å, and the bond lengths of Ca and neighboring O atoms are 2.056 Å, 2.222 Å, 2.203 Å, respectively. After modification of γ-Al$_2$O$_3$, the bond lengths between Cu and neighboring O atoms are 1.899 Å, 2.023 Å, 2.047 Å, the bond lengths between Mn and neighboring O atoms are 1.868 Å, 1.961 Å, 1.938 Å, and the bond lengths between Ni and neighboring O atoms are 1.868 Å, 1.881 Å, and 1.956 Å. In comparison, the bond lengths of Ca, Ce and neighboring O atoms are longer than those of Ca and Ce. In comparison, the bond
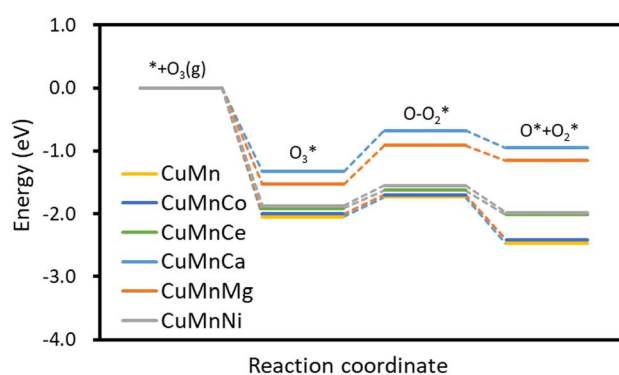

Fig. 7 Activation energy of O_3 catalyzed decomposition reaction of γ-Al$_2$O$_3$ modified by Cu/Mn/Co, Cu/Mn/Ce, Cu/Mn/Ca, Cu/Mn/Mg.

lengths of Ca and Ce with neighboring O atoms are longer than those of Co, Mg and Ni with neighboring O atoms.

The differential charge densities of Cu/Mn/Co, Cu/Mn/Ce, Cu/Mn/Ca, Cu/Mn/Mg, and Cu/Mn/Ni dopant-modified γ-Al$_2$O$_3$ were calculated by using the analysis program in the CASTEP module, and are shown in Fig. 3. Cu/Mn/Co, Cu/Mn/Ce,

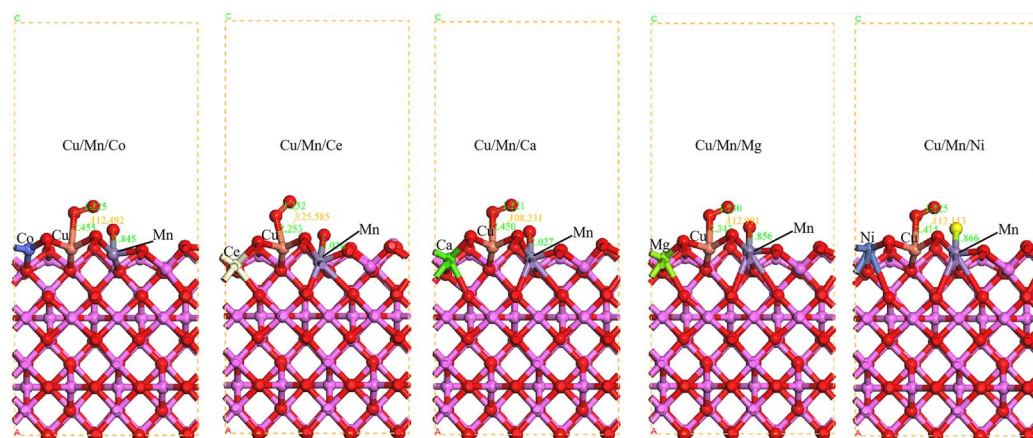**Fig. 6** Transition state configurations of γ-Al$_2$O$_3$ surface modified by Cu/Mn/Co, Cu/Mn/Ce, Cu/Mn/Ca, Cu/Mn/Mg and Cu/Mn/Ni doping.
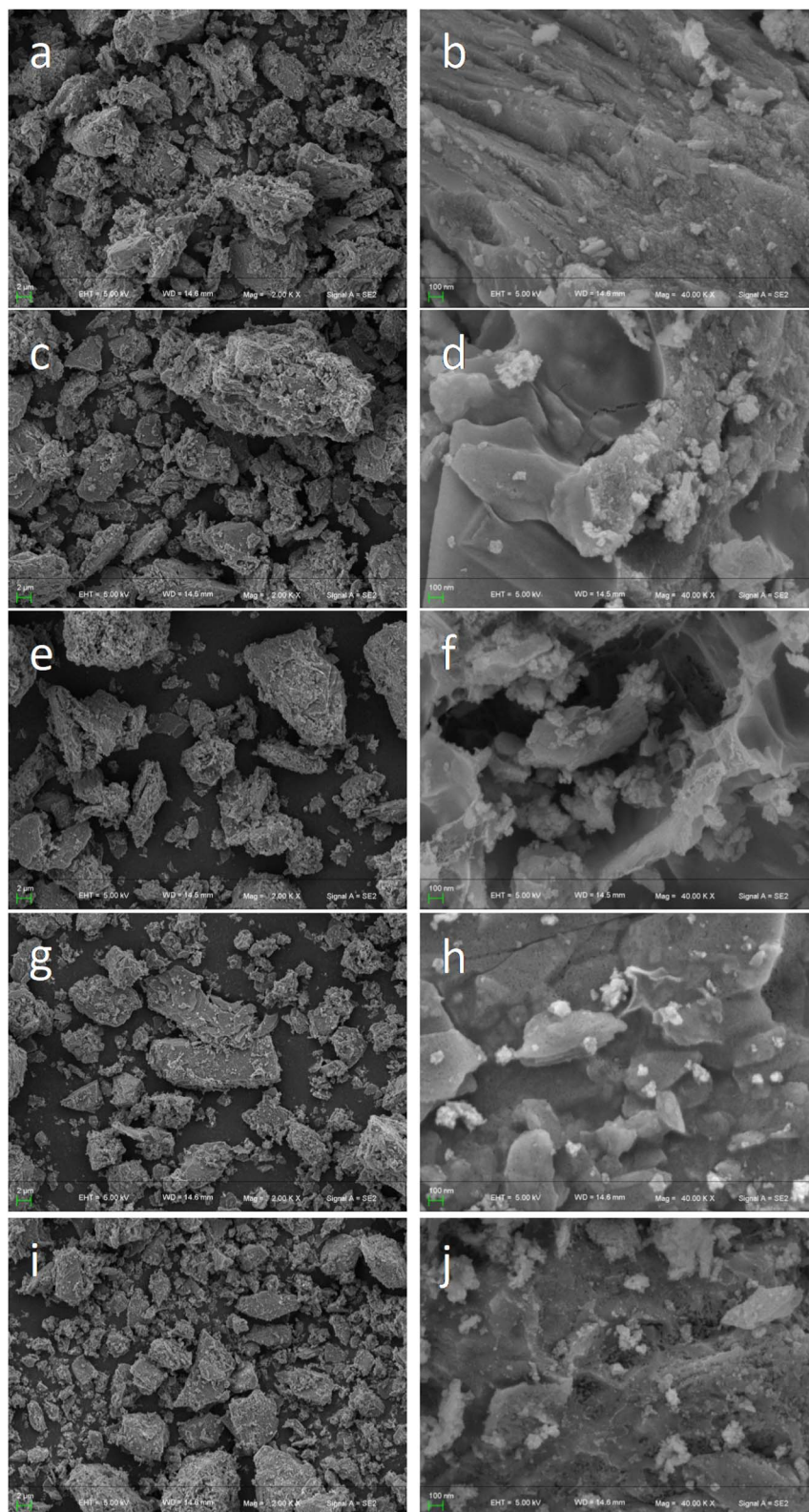
Fig. 8 SEM diagram. (a and b) 400 °C; (c and d) 500 °C; (e and f) 600 °C; (g and h) 700 °C; (i and j) 800 °C.

Cu/Mn/Ca, Cu/Mn/Mg, Cu/Mn/Ni doped modified γ-Al$_2$O$_3$ after the charge density difference is larger, Cu/Mn/Co and Cu/Mn/Ce doped modified γ-Al$_2$O$_3$ after the charge build-up effect is more pronounced, the charge of the Ce atoms to the O atoms to transfer more drastically, so that the O atoms around the charge density is higher, and is more conducive to the decomposition of the transformation of ozone.
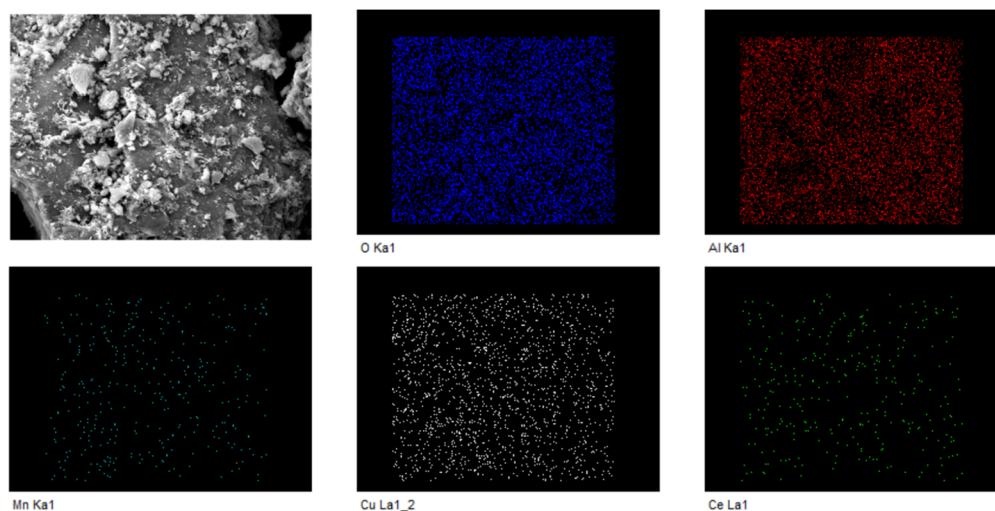
Fig. 9 EDS mapping diagram.

Table 1 Catalyst elemental composition

Element	Al	O	Mn	Cu	Ce
Content (%)	27.25	42.69	9.38	11.63	9.05

From the density-of-state diagram (Fig. 4), it can be seen that the active sites of Cu/Mn/Co and Cu/Mn/Ce doped modified γ-Al_2O_3 have strong peaks occupying the state near the Fermi energy level, and these two systems should have better catalytic activity. While the Ca and Mg doped systems do not have obvious peaks near the Fermi energy level, which indicates that the Ca and Mg doping is not conducive to the improvement of the catalytic performance. The Ni doping system has a weak peak near the Fermi energy level, indicating that the catalytic activity of the Ni doping system is average.

3.2 Comparison of ozone decomposition energy bases

The configurations of Cu/Mn/Co, Cu/Mn/Ce, Cu/Mn/Ca, Cu/Mn/Mg, Cu/Mn/Ni doped γ-Al_2O_3 adsorbed O_3 were

Table 2 BET test results of catalysts

Catalyst	Specific surface area ($m^2 g^{-1}$)
Cu/Mn/Ce–Al_2O_3-400 °C	218.27
Cu/Mn/Ce–Al_2O_3-500 °C	189.38
Cu/Mn/Ce–Al_2O_3-600 °C	185.02
Cu/Mn/Ce–Al_2O_3-700 °C	121.23
Cu/Mn/Ce–Al_2O_3-800 °C	60.69

constructed (Fig. 5). When O_3 was adsorbed on the surface of Cu/Mn/Ce doped γ-Al_2O_3, one of the O atoms of O_3 was bonded with Cu atoms with a bond length of 2.117 Å; another O atom of O_3 was bonded with Mn atoms with a bond length of 3.104 Å, and the angle of O atoms of O_3 was 116.54°. When O_3 is adsorbed on the surface of Cu/Mn/Ca-doped γ-Al_2O_3, one O atom of O_3 bonds with a Cu atom with a bond length of 2.117 Å, another O atom of O_3 bonds with a Mn atom with a bond length of 3.104 Å, and the O-atomic intersection angle of O_3 is 116.54°.
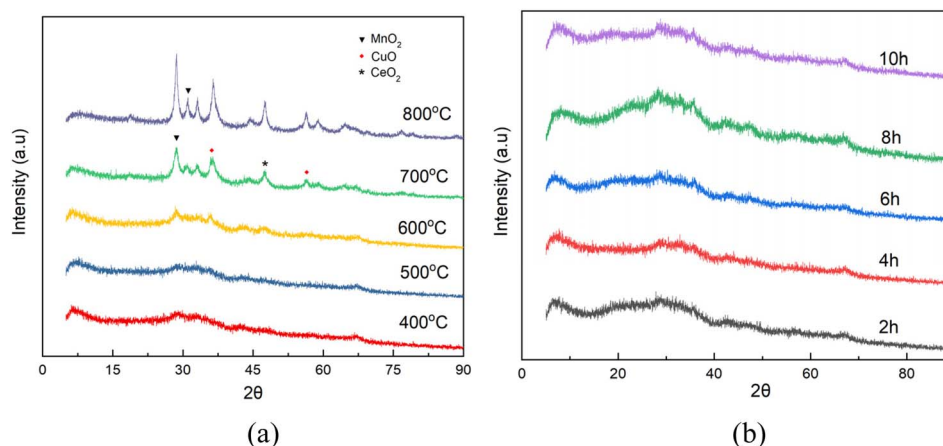

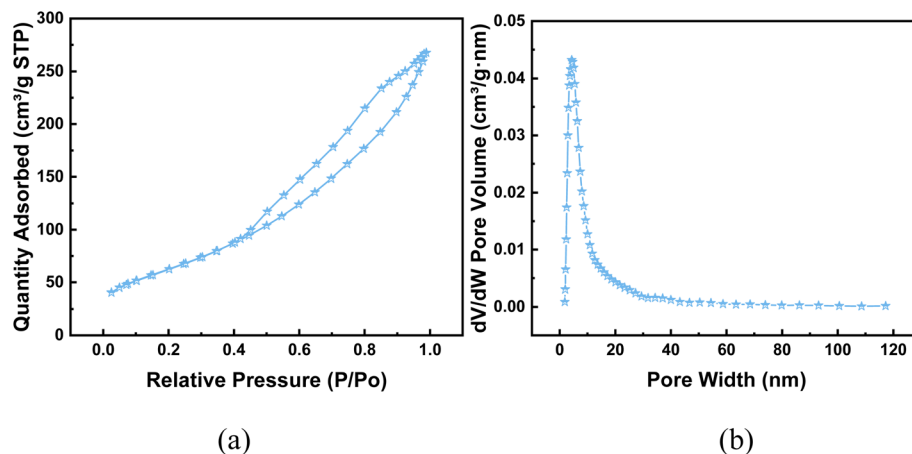**Fig. 10** XRD plots. (a) Different calcination temperatures; (b) different calcination times.

© 2024 The Author(s). Published by the Royal Society of Chemistry

Fig. 11 BET plots. (a) N_2 adsorption and desorption curve of catalyst (500 °C−4 h); (b) pore size distribution (500 °C−4 h).

When O_3 is adsorbed on the surface of Cu/Mn/Mg doped γ-Al_2O_3, one O atom of O_3 is bonded to a Cu atom with a bond length of 2.212 Å, another O atom of O_3 is bonded to a Mn atom with a bond length of 1.952 Å, and the O atomic interstitial angle of O_3 is 114.92°; when O_3 is adsorbed on the surface of Cu/Mn/Ni doped γ-Al_2O_3, one O atom of O_3 is bonded to a Cu atom with a bond length of 2.116 Å, and the O atomic interstitial angle of O_3 is 114.92°. When O_3 is adsorbed on the surface of Cu/Mn/Ni doped γ-Al_2O_3, one O atom of O_3 bonds with a Cu atom with a bond length of 2.116 Å; another O atom of O_3 bonds with a Mn atom with a bond length of 1.979 Å, and the O-atomic angle of O_3 is 114.91° (Fig. 6).

In the transition state of Cu/Mn/Co doped modified γ-Al_2O_3 surface O–O_2, the Cu–O bond length is 2.455 Å, the Mn–O bond length is 1.845 Å, which is longer than that of the adsorbed Cu–O and Mn–O bonds, and the O-atomic angle of the O_2 is 112.49°; in the transition state of Cu/Mn/Ce doped modified γ-Al_2O_3 surface O–O_2, the Cu–O bond length is 2.253 Å, the Mn–O bond length is 2.026 Å, which is longer than that of the adsorbed Cu–O and Mn–O bonds, and the O-atomic angle of the O_2 is 112.49°. O bond length is 2.253 Å and Mn–O bond length is 2.026 Å, which is longer than the Cu–O and Mn–O bonds in the adsorption state, and the O-atomic angle of O_2 is 125.59°; in the transition state of Cu/Mn/Ca doped and modified γ-Al_2O_3 surface O–O_2, the Cu–O bond length is 2.450 Å and Mn–O bond length is 2.027 Å, and the O-atomic angle of O_2 is 108.23°; the Cu/Mn/Ce doped and modified γ-Al_2O_3 surface O–O2 is 108.23°; the Cu/Mn/Ca doped and modified γ-Al_2O_3 surface O-atomic angle of O_2 is 108.23°. 108.23°; Cu/Mn/Mg dopant-modified γ-Al_2O_3 surface O–O_2 in the transition state, the Cu–O bond length is 2.343 Å, the Mn–O bond length is 1.856 Å, and the O-atomic angle of O_2 is 112.99°; Cu/Mn/Ni dopant-modified γ-Al_2O_3 surface O–O_2 in the transition state, the Cu–O bond length is 2.415 Å, the Mn–O bond length is 1.86 Å, the Mn–O bond length is 2.415 Å, the Mn–O bond length is 1.86 Å, the Mn–O bond length is 1.86 Å, the Mn–O bond length is 2.415 Å, and the Mn–O bond length is 1.86 Å. O bond length is 2.415 Å for Cu–O and 1.866 Å for Mn–O in the transition state, which is

longer than that of Cu–O and Mn–O in the adsorption state, and the O-atom angle of O_2 is 112.11° (Fig. 7).

The reaction energy barriers for catalytic O_3 decomposition on Cu/Mn/Co dopant-modified γ-Al_2O_3 surfaces are 0.30 eV, Cu/Mn/Ce dopant-modified γ-Al_2O_3 surfaces catalyze O_3 decomposition with a reaction energy barrier of −0.29 eV, Cu/Mn/Ca dopant-modified γ-Al_2O_3 surfaces catalyze O_3 decomposition with a reaction energy barrier of 0.65 eV, the reaction energy barrier of catalytic O_3 decomposition on Cu/Mn/Mg dopant-modified γ-Al_2O_3 surface is 0.62 eV, and the reaction energy barrier of catalytic O_3 decomposition on Cu/Mn/Ni dopant-modified γ-Al_2O_3 surface is 0.32 eV. The reaction energy barriers of catalytic O_3 decomposition on Cu/Mn/Co and Cu/Mn/Ce dopant-modified γ-Al_2O_3 surface were the lowest, all lower than 0.31 eV for Cu/Mn dopant-modified γ-Al_2O_3, and the reaction energy barriers of catalytic O_3 decomposition on the surface of Cu/Mn/Ni, Cu/Mn/Ca, and Cu/Mn/Mg dopant-modified γ-Al_2O_3 were higher than that of Cu/Mn dopant-modified γ-Al_2O_3, with the reaction energy barriers of catalytic O_3 decomposition on the surface of Cu/Mn/Ca and Cu/Mn/Mg dopant-modified γ-Al_2O_3 being higher than those of Cu/Mn dopant-modified γ-Al_2O_3. Al_2O_3 surface catalyzed O_3 decomposition with a reaction energy barrier as high as 0.62 eV, which may be caused by the introduction of Ca and Mg attenuating the adsorption of the catalyst on the product O + O_2, and the reaction thermodynamics is unfavorable due to the significant increase in the energy of the product, and the energy barrier is also elevated, and such a calculation is in agreement with the results of the analysis of the density of states. Therefore, Cu/Mn/Ce doped modified γ-Al_2O_3 was preferred as the ozone oxidation catalyst.

3.3 Catalyst characterization and performance verification

After optimization by simulation calculations, this work was carried out to prepare Cu/Mn/Ce dopant-modified γ-Al_2O_3 catalysts and analyze the catalyst morphology structure and chemical composition by a series of characterizations such as SEM, XRD, BET and XPS. For the Cu/Mn/Ce dopant-modified γ-Al_2O_3 catalysts calcined at 400–800 °C, the surface morphology

was compared, and the Cu/Mn/Ce dopant-modified γ-Al$_2$O$_3$ catalysts calcined at all temperatures had a good morphology structure, and the surface of the catalysts was rougher (Fig. 8). Meanwhile, the EDS scanning analysis results showed that the main active components Cu, Mn, and Ce were well dispersed without obvious agglomeration (Fig. 9), and the ratio of Cu, Mn, and Ce was close to 1 : 1 : 1 (Table 1), which was basically the same as that of the simulation optimization, and verified that the catalysts were successfully prepared. In addition, it can be seen from the XRD plots of calcination at 400–800 °C (the

retention time was 4 h, Fig. 10) that obvious characteristic peaks attributed to MnO$_2$, CuO, and CeO$_2$ oxides appeared in the range of $2\theta = 30$–60°, and the characteristic peaks were more sharp with the increase of temperature, indicating a good crystalline shape. However, when the effect of different calcination times was examined (the calcination temperature was 500 °C), it was found that there was no obvious effect of calcination time, therefore, for the metal oxide components, the calcination temperature is the main reason for determining their crystalline shape and activity. However, from the catalytic
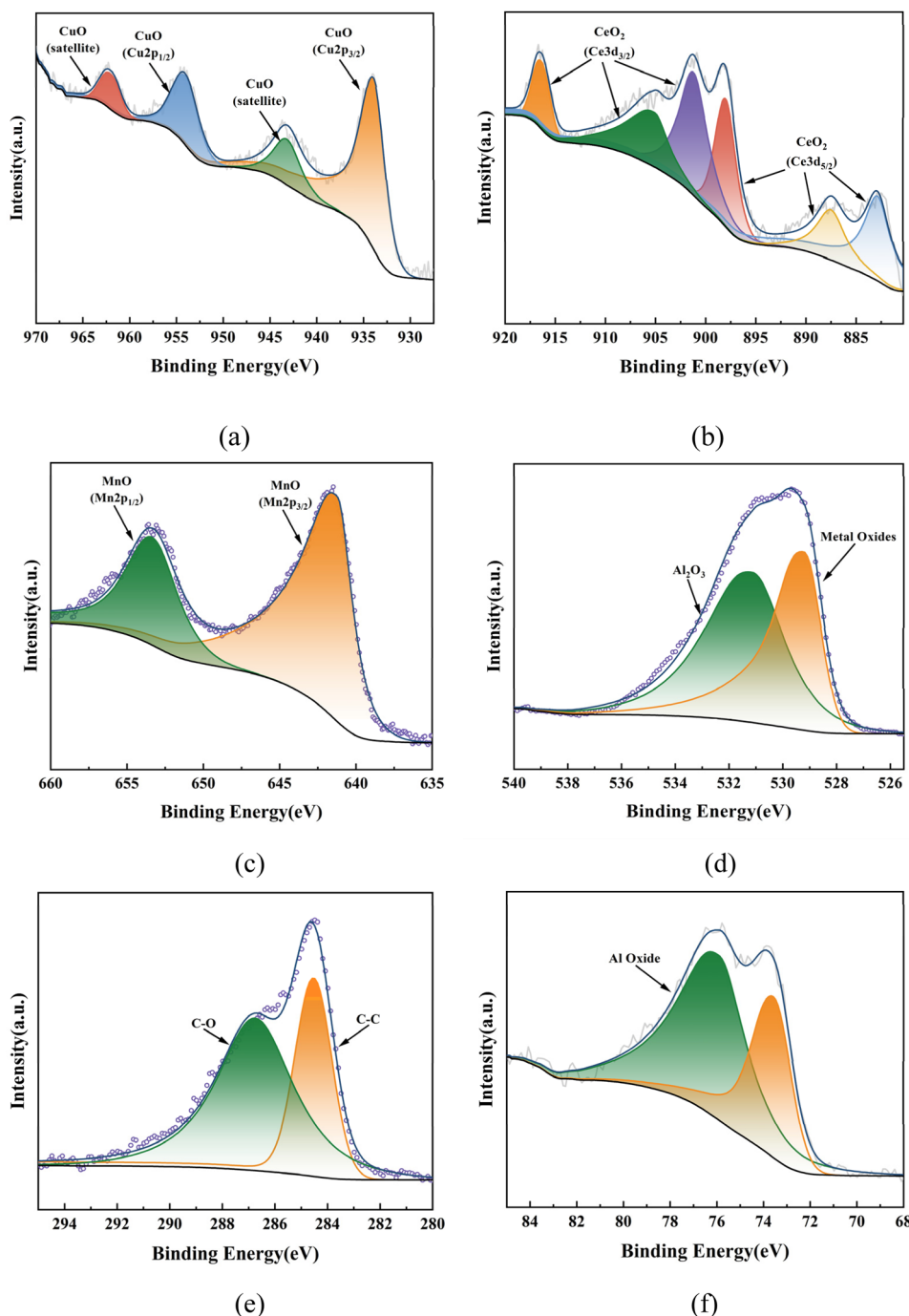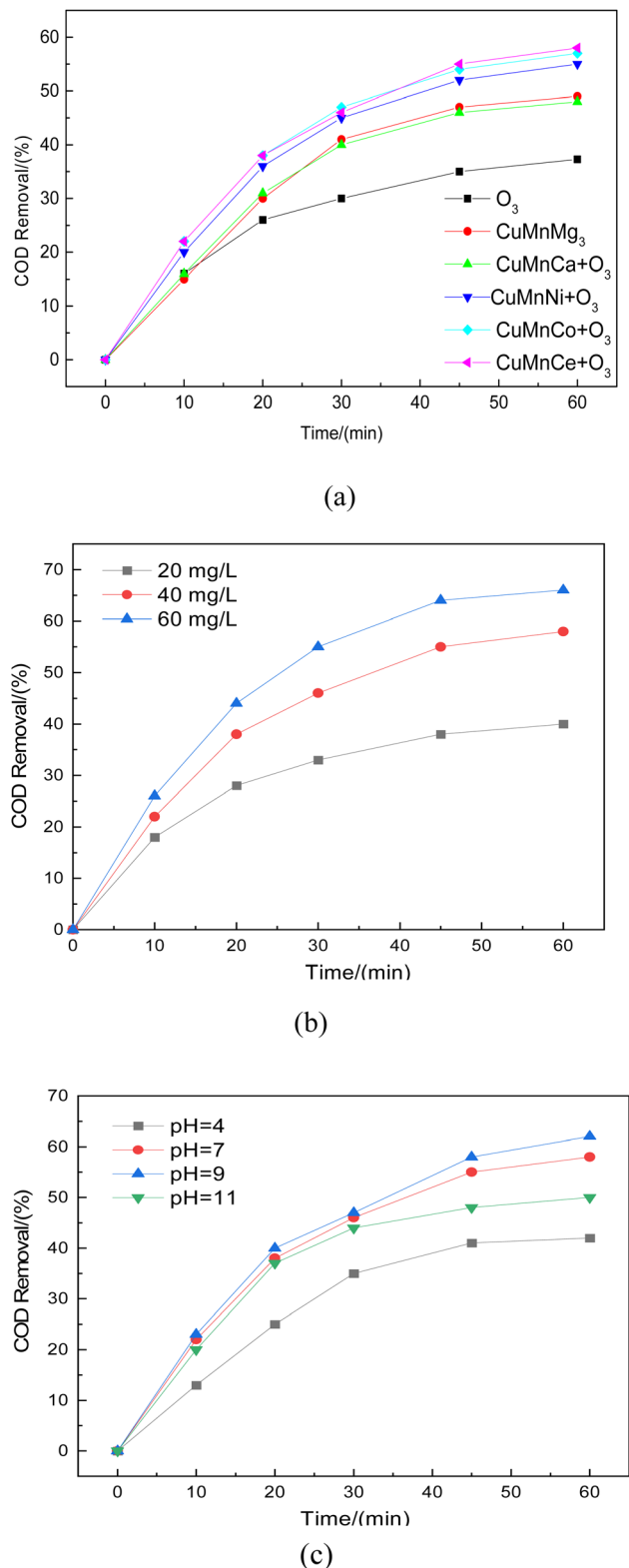

Fig. 12   XPS spectrogram.

Fig. 13 Catalyst performance validation. (a) Comparison of catalysts with different active components; (b) effect of ozone concentration on COD removal; (c) effect of different pH on COD removal.

oxidation process itself, the specific surface area of the catalyst itself is equally important, which determines the mutual contact of the catalyst active sites with ozone and pollutants. In the BET characterization, it is obvious that too high calcination temperature significantly affects the size of the surface area of the catalyst, especially the catalyst obtained by calcination at 700–800 °C, the specific surface area is only 80–120 m^2 g^{-1}, at this time, although the active component of metal oxides has a good crystalline shape, but the catalyst specific surface area is too small (Table 2), so the calcination temperature can be selected from 500–600 °C. What's more, the adsorption curve is of type III, and the pore size distribution is mainly in the range of 5–15 nm (Fig. 11), showing mesoporous distribution characteristics.[25,26] Finally, this work further verified the catalyst metal oxide active component species by XPS analysis (Fig. 12), the presence of the elements Mn, Cu, O and Ce was confirmed,[27–29] which is consistent with the SEM-EDS results. The Cu active fraction mainly exists in the form of CuO (Fig. 12a), the Ce active fraction mainly exists in the form of CeO_2 (Fig. 12b), and the Mn active fraction mainly exists in the form of MnO (Fig. 12c). Meanwhile, the split-peak profiles of Al, O, and C proved the presence of Al_2O_3 (Fig. 12d–f).

After the successful preparation of the catalyst was clarified by a series of characterizations such as SEM, XRD, BET, and XPS, this work mainly investigated the effect of different metal components on the catalyst activity and the variation of COD removal rate under different ozone concentrations and pH environments, and the results are shown in Fig. 13. The COD removal of the ozone oxidation process alone could reach about 35%. Compared with the ozone oxidation process alone, the COD removal rate was significantly increased by the addition of CuMnMg, CuMnCa, CuMnNi, CuMnCo, and CuMnCe catalysts. Among them, the COD removal rate of the ozone-catalyzed oxidation process dominated by CuMnMg and CuMnCa catalysts was about 50%, whereas the COD removal rate of the ozone oxidation process dominated by CuMnNi, CuMnCo, and CuMnCe catalysts was more than 55%, and in particular, the COD removal rate of the oxidation process dominated by CuMnCe catalysts was up to 60%, which indicated that the introduction of Ce introduction is the most significant improvement of catalyst activity (Fig. 13a), which is consistent with the simulation results. The main reason may be that CeO_2 has more abundant lattice oxygen, which is more favorable for the ozone catalytic oxidation process. At the same time, when the ozone concentration was gradually increased from 20 mg L^{-1} to 60 mg L^{-1}, the COD removal rate was significantly increased, up to about 65%, which was mainly due to the fact that under high ozone concentration, the catalyst active sites could catalyze the formation of more active radicals from ozone. However, the increase of COD removal was small when the ozone concentration was increased from 40 mg L^{-1} to 60 mg L^{-1}. Therefore, an ozone concentration of 40 mg L^{-1} was chosen, and the catalysts showed good catalytic activity under different pH environments, but it was obvious that the acidic environment inhibited the COD removal, which was mainly due to the fact that the acidic environment was unfavorable to the generation of free radicals. At the same time, the strong alkalinity at pH = 11 was destructive to the original good morphological structure of the catalyst, which was also detrimental to the catalytic oxidation process of ozone. Therefore, the catalyst has better catalytic activity when the pH of wastewater is 7–9 (Fig. 13c).
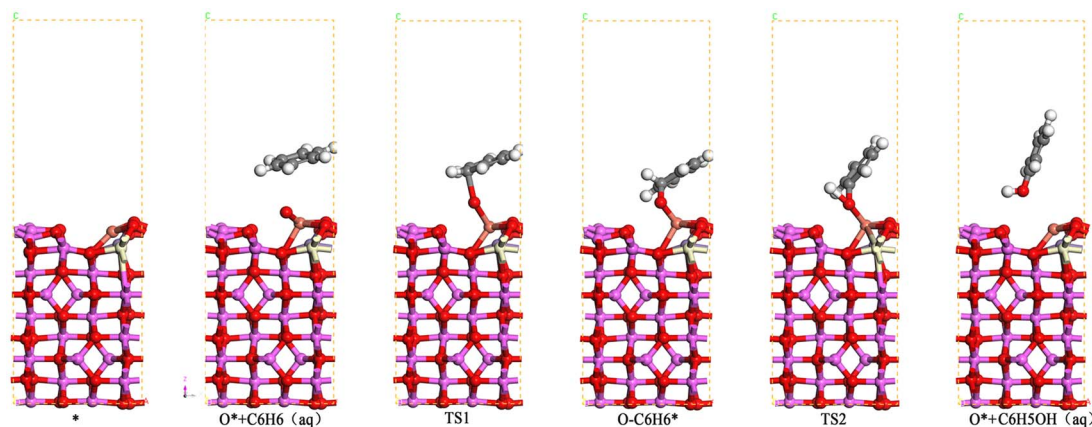
Fig. 14 Reaction configuration of benzene catalyzed oxidation by γ-Al$_2$O$_3$ modified by Cu/Mn/Ce doping.

3.4 Catalyst mechanism study

When benzene was used as a simulated pollutant in the catalytic oxidation of benzene, the active metal on the surface of the Cu/Mn/Ce doped modified γ-Al$_2$O$_3$ catalyst firstly adsorbed O$_3$ to form the adsorption state O*, and then bonded with benzene's C-atoms to form O* + C$_6$H$_6$(aq), and then through the transition state to form the adsorption state O–C$_6$H$_6$*, and then transformed O–C$_6$H$_6$* into C$_6$H$_5$OH(aq) (Fig. 14). Among them, the reaction energy for the transformation of O* + C$_6$H$_6$ (aq) to O–C$_6$H$_6$* is 0.52 eV, and the reaction energy for the transformation of O–C$_6$H$_6$* to C$_6$H$_5$OH (aq) is 0.61 eV, so the step of the transformation of O–C$_6$H$_6$* to C$_6$H$_5$OH (aq) is a rate-controlling step, and according to the Arrhenius formula, if the energy barrier of a reaction is lower than 0.7 eV, then the reaction can be carried out at room temperature. Therefore, the Cu/Mn/Ce-modified γ-Al$_2$O$_3$ can oxidize benzene to phenol and further degrade to carbon dioxide and water. Meanwhile, the free radical species for its ozone-catalyzed oxidation process by EPR (Fig. 16). 5,5-Dimethyl-1-pyrroline N-oxide(DMPO) was used as the scavenger of hydroxyl radicals and superoxide radicals, and 2,2,6,6-tetramethyl-1-piperidinyloxy (TEMP) was used as the scavenger of single-linear oxygen, and the results are shown in Fig. 15. Superoxide radicals and single-linear oxygen mainly existed in the ozone-catalyzed oxidation process dominated by Cu/Mn/Ce-modified γ-Al$_2$O$_3$ catalysts, and the characteristic signals of

hydroxyl radical were the weakest, which indicated that superoxide radicals and single-linear oxygen dominated the oxidative degradation of organic pollutants.

3.5 Catalyst stability evaluation

6 kg of catalyst was prepared by granulation method and loaded into a 20L h^{-1} ozone catalytic oxidation continuous unit reactor (Fig. 17) to simulate the initial concentration of wastewater COD of about 250 mg L^{-1}. The catalyst limit performance test and catalyst stability test were carried out respectively.

As shown in Fig. 17, with the reaction, the COD removal rate in the stage is more stable, about 55% (during 300 h of operation), indicating that the performance of the catalyst is stable, and has the prospect of industrial application.

3.6 The potential industrial applications and scalability of catalyst

The catalysts prepared in this work can be prepared at a scale of 2–5 kg in a single run in the laboratory, while the preparation process is simple and mature, and the catalysts are easy to be
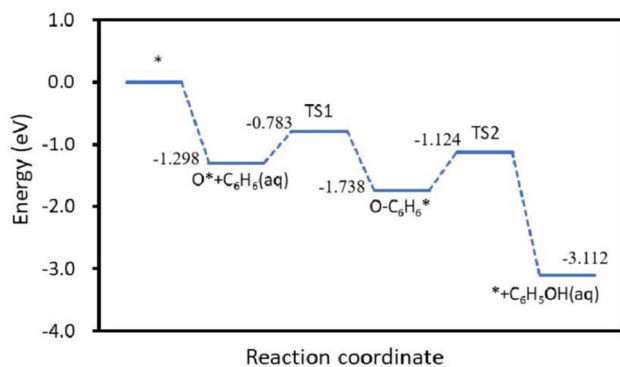

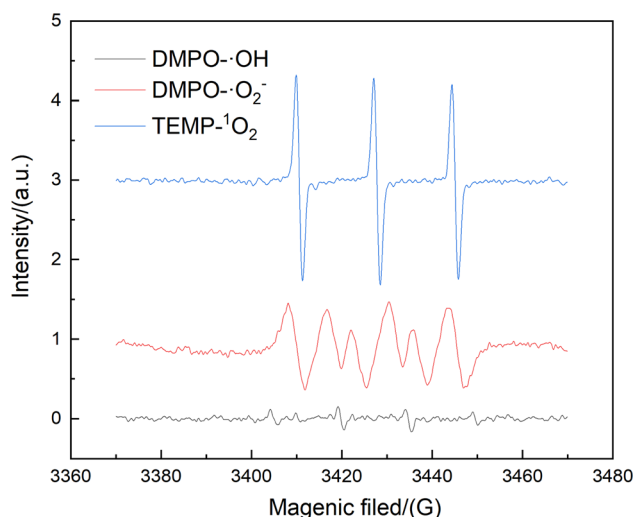**Fig. 15** Benzene catalyzed oxidation reaction path by γ-Al$_2$O$_3$ modified by Cu/Mn/Ce doping.
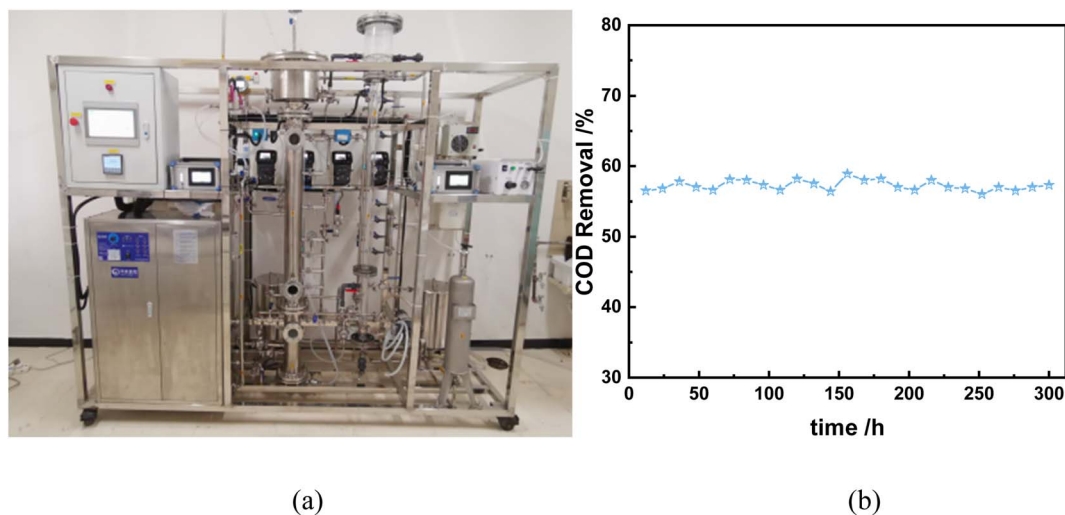

Fig. 16 EPR mapping.

(a)

(b)

Fig. 17 (a) Catalyst and 20 L h^{-1} ozone catalytic oxidation continuous unit; (b) continuous test COD monitoring. (Condition: inlet water flow 10 L h^{-1}, O$_3$ flow 0.4 L min^{-1}, O$_3$ concentration 40 mg L^{-1}, retention time 30 min, sampling every 12 h to measure COD.)

prepared on a large scale. Meanwhile, through the stability test of the catalyst, its performance basically remains unchanged, indicating that it has good stability. Therefore, the prepared catalysts have stable performance and little difficulty in large-scale preparation, and have the potential for industrial application.

4. Conclusion

In this work, an efficient Cu/Mn/Ce multi-metal oxide composite catalyst was designed and synthesized by metal salt precursor mixing-direct granulation. Systematic characterization by XRD, XPS and BET combined with DFT calculations revealed the constitutive relationship of the catalyst, and Cu/Mn/Ce was the main active metal component of the catalyst, and the COD removal could reach more than 50% for the simulated wastewater and the catalyst activity remained basically stable for a long period of 1000 h. The EPR characterization clarified that the degradation of organic pollutants in the catalytic process was mainly dominated by single-linear oxygen and superoxide radicals, and proposed a possible catalytic oxidation mechanism, which provided a reference for the synthesis of new efficient ozone oxidation catalysts and the deep treatment of wastewater.

Data availability

The authors declare that the data will be made available on request.

Conflicts of interest

The authors declare no competing interests.

Acknowledgements

References

1 Q. Li, Y. Wang, Z. Chang, *et al.*, Progress in the treatment of copper (II)-containing wastewater and wastewater treatment systems based on combined technologies: A review, *J. Water Proc. Eng.*, 2024, **58**, 104746.

2 J. Bi and G. Dong, Wastewater Treatment: Functional Materials and Advanced Technology, *Molecules*, 2024, **29**(9), 2150.

3 Y. Wang, H. Li, J. Xu, *et al.*, High-performance carbon@metal oxide nanocomposites derived metal–organic framework-perovskite hybrid boosted microwave-induced catalytic degradation of norfloxacin: performance, degradation pathway and mechanism, *Sep. Purif. Technol.*, 2024, **330**, 125399.

4 Y. Wang, N. Lin, J. Xu, *et al.*, Construction of microwave/PMS combined dual responsive perovskite-MXene system for antibiotic degradation: synergistic effects of thermal and non-thermal, *Appl. Surf. Sci.*, 2023, **639**, 158263.

5 B. Gao, X. Feng, Y. Zhang, *et al.*, Graphene-based aerogels in water and air treatment: a review, *Chem. Eng. J.*, 2024, 149604.

6 J. Wei, Y. Zhang, Z. Zhou, *et al.*, PVP-modified spindle-shaped MIL-88B (Fe) to enhance the degradation of tetracycline by activated peroxodisulfate: a comparative study and mechanistic investigation, *Prog. Nat. Sci.: Mater. Int.*, 2023, **33**(6), 872–880.

7 N. Liu, D. Wang, J. Xu, *et al.*, Novel 3D MIL-53 (Fe)/graphene aerogel composites for boosted photocatalytic ibuprofen degradation under visible light: process and mechanism, *Surf. Interfaces*, 2024, **46**, 104192.

8 A. Buthiyappan and A. A. A. Raman, Energy intensified integrated advanced oxidation technology for the treatment of recalcitrant industrial wastewater, *J. Cleaner Prod.*, 2019, **206**, 1025–1040.

9 M. S. Nawaz and M. Ahsan, Comparison of physico-chemical, advanced oxidation and biological techniques for the textile wastewater treatment, *Alexandria Eng. J.*, 2014, **53**(3), 717–722.

10 Y. Cheng, Z. Chen, S. Wang, *et al.*, Single atom catalysts for heterogeneous catalytic ozonation, *Curr. Opin. Chem. Eng.*, 2023, **41**, 100945.

11 M. Bilińska, L. Bilińska and M. Gmurek, Homogeneous and heterogeneous catalytic ozonation of textile wastewater: application and mechanism, *Catalysts*, 2022, **13**(1), 6.

12 Z. Cheng, R. Yang, B. Wang, *et al.*, Chlorophenol degradation in papermaking wastewater through a heterogeneous ozonation process catalyzed by Fe-Mn/sepiolite, *BioResources*, 2015, **10**(3), 5503–5514.

13 A. Araújo, O. Soares, C. A. Orge, *et al.*, Metal-zeolite catalysts for the removal of pharmaceutical pollutants in water by catalytic ozonation, *J. Environ. Chem. Eng.*, 2021, **9**(6), 106458.

14 S. Khuntia, M. K. Sinha and P. Singh, Theoretical and experimental investigation of the mechanism of the catalytic ozonation process by using a manganese-based catalyst, *Environ. Technol.*, 2021, **42**(4), 632–639.

15 X. Li, W. Chen, L. Ma, *et al.*, Industrial wastewater advanced treatment *via* catalytic ozonation with an Fe-based catalyst, *Chemosphere*, 2018, **195**, 336–343.

16 Z. Huangfu, W. Ju, Y. Jia, *et al.*, A novel insight of degradation ibuprofen in aqueous by catalytic ozonation with supported catalyst: supports effect on ozone mass transfer, *J. Environ. Sci.*, 2024, **145**, 216–231.

17 J. Wang and H. Chen, Catalytic ozonation for water and wastewater treatment: recent advances and perspective, *Sci. Total Environ.*, 2020, **704**, 135249.

18 G. Wang, L. Kou, M. Liu, *et al.*, Application advance of combined technology of Micro-Nano Bubbles and catalytic ozonation, *Coal Qual. Technol.*, 2023, **38**, 21–28.

19 D. Yang, F. Meng, Z. Zhang, *et al.*, Enhanced Catalytic Ozonation by Mn–Ce Oxide-Loaded Al_2O_3 Catalyst for Ciprofloxacin Degradation, *ACS Omega*, 2023, **8**(24), 21823–21829.

20 B. Zhou, X. Zhang, P. Wang, *et al.*, Application of metal oxide catalysts for water treatment – a review, *J. Mol. Liq.*, 2024, 124644.

21 W. Yang, B. Vogler, Y. Lei, *et al.*, Metallic ion leaching from heterogeneous catalysts: an overlooked effect in the study of catalytic ozonation processes, *Environ. Sci.: Water Res. Technol.*, 2017, **3**(6), 1143–1151.

22 C. Chen, N. Jia, K. Song, *et al.*, Sulfur-doped copper-yttrium bimetallic oxides: a novel and efficient ozonation catalyst for the degradation of aniline, *Sep. Purif. Technol.*, 2020, **236**, 116248.

23 L. Li, R. Fu, J. Zou, *et al.*, Research progress of iron-based catalysts in ozonation wastewater treatment, *ACS ES&T Water*, 2023, **3**(4), 908–922.

24 H. Wang, M. S. Bootharaju, J. H. Kim, *et al.*, Synergistic interactions of neighboring platinum and iron atoms enhance reverse water–gas shift reaction performance, *J. Am. Chem. Soc.*, 2023, **145**(4), 2264–2270.

25 B. Gao, F. Bi, Z. Zhou, *et al.*, A bimetallic MOF-derived MnCo spinel oxide catalyst to enhance toluene catalytic degradation, *Chem. Commun.*, 2024, **60**(58), 7455–7458.

26 F. Bi, S. Ma, B. Gao, *et al.*, Boosting toluene deep oxidation by tuning metal-support interaction in MOF-derived $Pd@ZrO_2$ catalysts: the role of interfacial interaction between Pd and ZrO_2, *Fuel*, 2024, **357**, 129833.

27 X. Zhang, R. Rao, B. Gao, *et al.*, Crystal engineering of TiO_2 enhanced photothermal catalytic degradation of DEHP on Pt catalysts, *Mater. Today Chem.*, 2023, **34**, 101755.

28 F. Bi, X. Feng, Z. Zhou, *et al.*, Mn-based catalysts derived from the non-thermal treatment of Mn-MIL-100 to enhance its water-resistance for toluene oxidation: Mechanism study, *Chem. Eng. J.*, 2024, **485**, 149776.

29 X. Zhang, F. Bi, Z. Zhu, *et al.*, The promoting effect of H_2O on rod-like $MnCeO_x$ derived from MOFs for toluene oxidation: a combined experimental and theoretical investigation, *Appl. Catal., B*, 2021, **297**, 120393.